INORGANIC CHEMISTRY
FRONTIERS

RESEARCH ARTICLE

View Article Online
View Journal | View Issue

Cite this: *Inorg. Chem. Front.*, 2023, **10**, 2294

Inhibiting Li^+ migration by thenoyltrifluoroacetone toward efficient and stable perovskite solar cells†

Yuting Ma,[a] Gaoyi Han, *[a] Meiling Yang,[a] Mengna Guo,[a] Yaoming Xiao,*[b] Yao Guo *[c] and Wenjing Hou *[a]

Received 20th November 2022,
Accepted 18th March 2023

DOI: 10.1039/d2qi02460h

rsc.li/frontiers-inorganic

Lithium bis(trifluoromethanesulfonyl)imide is commonly employed as a dopant to improve the hole mobility of hole transport layers. However, undesired Li^+ migration impedes the development of highly efficient and stable perovskite solar cells because the voids left by Li^+ migration will accelerate the penetration of oxygen and moisture. Here, thenoyltrifluoroacetone (TTA) modifies the perovskite/spiro-OMeTAD interface. TTA can passivate the undercoordinated Pb^{2+} defects *via* the coordination between carbonyl/thiophenic sulfur and Pb^{2+}. TTA can also inhibit the annoying Li^+ migration by the coordination interaction between carbonyl and Li^+. Besides, TTA can promote hole extraction by adjusting the energy level matching at the perovskite/hole transport layer interface. A TTA-modified device yields a power conversion efficiency of over 22% and has improved humidity and thermal stability. This finding paves a novel way to suppress undesired Li^+ migration for highly efficient and stable PSCs.

Introduction

Remarkable achievements in organic–inorganic hybrid perovskite solar cells (PSCs) have been attained in recent years, with a power conversion efficiency (PCE) of 25.7% owing to their brilliant optoelectronic properties, including huge light absorption, mensurable band gap, long charge carrier diffusion length and so on.[1,2] Among all the device structures, PSCs with the formal n-i-p structure have been widely developed and shown significant commercial potential due to their simple fabrication and high efficiency. It is worth noting that the hole transport layer (HTL) plays a crucial role in improving hole transport and conversion efficiency, and in preventing electron reverse transport.[3]

Among many HTL materials, 2,2′,7,7′-tetrakis(*N*,*N*-di-*p*-methoxyphenlamine)-9,9′-spirobifluorene (spiro-OMeTAD) has an irreplaceable role because of its large band gap, deep HOMO level, high glass transition temperature and melting point, and some amorphous properties.[4] However, pure spiro-OMeTAD has two fundamental drawbacks: low hole mobility and low electrical conductivity.[5] Thus, researchers use lithium bistrifluoromethanesulfonimide (Li-TFSI) and 4-*tert*-butylpyridine (TBP) as additives to improve the hole mobility and conductivity of spiro-OMeTAD.[5] Although the addition of Li-TFSI can improve the performance of the HTL, the super hygroscopicity of Li-TFSI always leads to its self-agglomeration, which results in a decrease in device efficiency and stability by affecting the performance of the HTL.[6] In addition, Li^+ is prone to migrate and diffuse into the matrix due to its small radius and high ion mobility.[7] When the device is under working conditions, Li^+ is driven by the electric field and migrate from the HTL to the perovskite layer, forming the hygroscopic LiX (X = Cl^-, Br^-, and I^-).[8] Meanwhile, the migration paths of Li^+ at the perovskite/HTL interface and perovskite layer provide intrusion access for water molecules and oxygen, which accelerate the degradation of the perovskite film from the interface to the bulk phase.[9] Recent studies also revealed that Li^+ migration is one of the most dominant factors causing the degradation in device performances, especially in spiro-OMeTAD-based PSCs.[6] Therefore, it is of practical significance to study the effective strategies to inhibit the action of Li^+ migration at the perovskite/HTL interface for improving the stability of perovskite solar cells.

As of this writing, three main strategies have emerged to inhibit Li^+ migration for enhancing the PCE and stability. First, synthesis of new hole-transporting materials that can coordinate with Li^+. Li *et al.* have modified hole transport layer materials with Lewis bases (such as pyridine, 1,10-phenanthro-

---

[a] *Institute of Molecular Science, Key Laboratory of Chemical Biology and Molecular Engineering of Education Ministry, Key Laboratory of Materials for Energy Conversion and Storage of Shanxi Province, Shanxi University, Taiyuan 030006, P. R. China. E-mail: han_gaoyis@sxu.edu.cn, wjhou2016@sohu.com*

[b] *College of Chemical Engineering and Materials Science, Quanzhou Normal University, Quanzhou 362000, P. R. China. E-mail: ymxiao@qztc.edu.cn*

[c] *School of Materials Science and Engineering, Henan Joint International Research Laboratory of Nanocomposite Sensing Materials, Anyang Institute of Technology, Anyang 455000, P. R. China . E-mail: Guoyao@ayit.edu.cn*

† Electronic supplementary information (ESI) available: Experimental procedures, device fabrication details and characterization. See DOI: **https://doi.org/10.1039/d2qi02460h**

line and pyrazine) *via* a covalent connection method,[10] and the results have indicated that these Lewis bases can suppress the Li^+ migration by coordinating with Li^+ ions. Park *et al.* have reported a novel organic HTL material (HL38) with a D–π-A–π-D structure, which can inhibit Li^+ migration by using the strong coordination between –C=O and Li^+ in HL38.[6] Second, dopants that can effectively replace Li-TFSI are selected. Jia *et al.* have used fluorinated Fe(F20TPP)Cl as an alternative to Li-TFSI to dope spiro-OMeTAD, and a device fabricated with Fe(F20TPP)Cl dopant achieved a device efficiency of more than 21% and good long-term stability due to the dopant's hydrophobic properties and higher migration barrier.[11] Furthermore, this is also an effective strategy to replace Li^+ from Li-TFSI by other cations with lower mobility. These researchers have replaced the Li-TFSI dopant with Zn-$TFSI_2$, TBA-TFSI (TBA = tetrabutylammonium), Mg-$TFSI_2$ and Ca-$TFSI_2$, which improved the corresponding device efficiency and environmental stability.[12–14] Third, capturing the Li^+ ions in a doped HTL. Li *et al.* have utilized the host–guest interaction between 12-crown-4 and Li^+ to form a more stable and less diffused crown ether–Li complex, which could delay the generation of hygroscopic lithium oxides and slow down the migration of Li^+.[15] Yang *et al.* have used the 2D graphite carbon nitride nanosheets (CNVx) as a dopant of spiro-OMeTAD to confine the movement of Li^+ and significantly improve the conductivity and hole mobility of HTL films.[16] In addition to the structural design and modification aimed at the HTL itself and its dopant composition, selecting suitable Li^+ migration inhibitors to modify and regulate the interface between the perovskite and HTL layer is also a potential method to inhibit Li^+ migration.[17]

Besides Li^+ migration, there exist potential barriers at the perovskite/spiro-OMeTAD interface, which lead to energy loss and the impeding of hole extraction.[18] Choosing suitable Li^+ migration inhibitors as interface modifiers can not only inhibit Li^+ migration, but can also take the stability and charge extraction properties of the perovskite/HTL interface into consideration, which is of great significance for further improving device stability. Therefore, the ideal Li^+ migration inhibitor should meet the following requirements: (i) it should passivate the defects of perovskite and have no negative effects on the formation of HTL film; (ii) it can effectively regulate the energy level structure at the perovskite/HTL interface to improve the interface hole extraction efficiency; (iii) it should contain the Li^+ binding sites to effectively inhibit Li^+ migration that starts from the perovskite/HTL interface; and (iv) it should possess excellent stability to enhance the interface and device stability.

Thenoyltrifluoroacetone (TTA) is a β-diketone small molecule, which is commonly used as the reagent for extraction and separation of metal ions, especially Li^+. Carbonyl groups in TTA can form stable chelating structures with small-radius Li^+ through interaction between the hybrid sp3 orbital of Li^+ and the β-diketone,[19] which has the potential to inhibit Li^+ migration. Meanwhile, the carbonyl (–C=O) and thienyl groups in TAA can anchor the uncoordinated Pb^{2+} ions in perovskite; the –C=O and –F groups can form hydrogen bonding with the organic amine fraction in perovskite; and the enhanced interaction between TTA and perovskite can reduce the trap density and related recombination, promoting charge transport at the interface of the perovskite and spiro-OMeTAD. Targeting the problem of Li^+ migration and possible losses at the perovskite/HTL interface, we demonstrate the use of TTA as an interfacial modifier to inhibit Li^+ migration while also considering the morphology of the perovskite film and the extraction of interfacial charge. Without employing any conventional passivator, the PCE of the best device using TTA as a modifier is 22.03%, which is significantly higher than that of the control device (20.17%). Notably, TTA-modified devices maintain 69.12% and 63.35% of their initial efficiency after aging under air conditions of 50%–60% RH and after being heated at 60 °C in an Ar-filled glove box for 700 h, respectively.

Results and discussion

Fig. 1a shows the n-i-p planar photovoltaic device structure decorated with TTA, where the isopropyl alcohol solution of TTA was spin-coated on the $(FA_{0.54}MA_{0.41}Cs_{0.05})Pb(I_{0.98}Br_{0.02})_3$ perovskite film. Fig. 1b shows the electrostatic potential map and structure of TTA, where the potential on the carbonyl is the most negative and the electron cloud is the densest. Compared with –C=O, the thiophene S has the second highest electron cloud density. These results mean that the carbonyl and thiophene S are more likely to provide electrons to coordinate with metal ions. The effects of TTA interface modification on the morphologies of perovskite were investigated by field emission scanning electron microscopy (FESEM) characterization. In Fig. 1c, d and Fig. S1,† after TTA modification, the grain size of perovskite increases, and 0.4 M TTA-modified perovskite film shows the largest average grain size of 756 nm, which indicates that TTA has the potential to improve the quality of perovskite films. The isopropyl alcohol (IPA) solvent used for dissolving TTA can slightly dissolve the perovskite components, which makes it possible for TTA to promote the secondary growth of perovskite grains based on the possible coordination roles. In Fig. 1e and f, the energy dispersive X-ray spectroscopy (EDS) mappings of F and O elements show that TTA is uniformly distributed on the surface of the perovskite film. In addition, the same peak positions of X-ray diffraction (XRD) in Fig. 1g showed that TTA will not enter into the perovskite lattice, but the intensity of PbI_2 was weakened after TTA modification, indicating that the TTA could react with the PbI_2. Previous reports have also interpreted that moderated PbI_2 is conducive to passivate the defects at the grain boundary.[20] Fig. 1h also shows that TTA helps to improve the light absorbance of perovskite films, which indicates that more light can be utilized for photoelectric conversion. Fig. 1i and j show that TTA modification would not exert negative effects on the formation of spiro-OMeTAD films. In Fig. 1k and l, compared with the control perovskite film with the cross-sectional thickness of 493 nm,

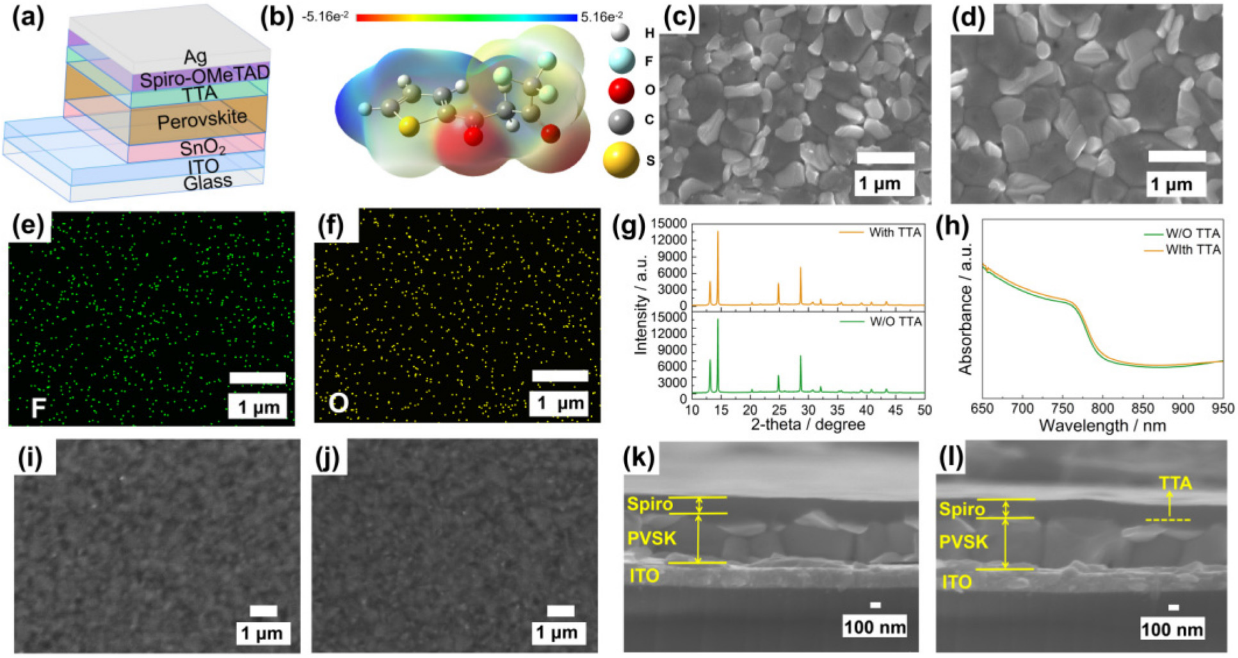

Fig. 1 (a) TTA-modified device structure; (b) electrostatic potential (ESP) mapped onto the total electron surface of TTA; top-view SEM images of (c) control and (d) TTA-modified perovskite films; EDS images for (e) F and (f) O elements from TTA-modified perovskite film; (g) XRD patterns and (h) UV-vis absorbance spectra of perovskite films; top-view SEM images of spiro-OMeTAD film (i) without (W/O) TTA and (j) with TTA modification; cross-sectional SEM images of the device (k) W/O TTA and (l) with TTA modification.

the TTA-modified perovskite film exhibited a slightly increased thickness of 500 nm, which can explain the increased light absorbance in Fig. 1h.

The interaction mechanisms of TTA at the perovskite/HTL interface were studied by using Fourier transform infrared spectra (FTIR). In Fig. S2a and b,† after interacting with the perovskite, the wavenumber of –C–S in TTA shifts from 731 cm^{-1} to 726 cm^{-1},[21] and the wavenumber of –C=O in TTA shifts from 1658 cm^{-1} to 1619 cm^{-1},[22] respectively. The reduced wavenumber results from the weakened –C–S and –C=O bonds by possible coordination for –C–S···Pb and –C=O···Pb. Besides, in Fig. S3,† the stretching vibration peak of –N–H in the perovskite moved from 3391 cm^{-1} to the high wavenumber of 3397 cm^{-1} after TTA modification, indicating the possible hydrogen bonding interaction between the perovskite and TTA by forming the –C=O···H and –F···H bonds.[21] X-ray photoelectron spectroscopy (XPS) was used to characterize the interaction between TTA and the perovskite further. In Fig. 2a, the binding energy of Pb $4f_{7/2}$ (138.21 eV) and Pb $4f_{5/2}$ (143.09 eV) for the perovskite shifted to 137.74 eV and to 142.55 eV for the TTA-modified perovskite, respectively.[23] In Fig. 2b and c, for the TTA-modified perovskite, the binding energy of O 1s in TTA (529.79 eV) shifted to 530.98 eV, and the binding energy of S $2p_{1/2}$ (169.54 eV) and S $2P_{3/2}$ (168.40 eV) from the thiophene ring shifted to 169.79 eV and 168.55 eV, respectively.[21] The low-shifted binding energy of Pb 4f and high-shifted binding energy of –C=O and thiophene S show that the thiophene S and –C=O group in TTA can passivate the uncoordinated Pb^{2+} defect by donating their electrons to Pb. The chemical interaction between TTA and the perovskite was further studied by employing density functional theory (DFT) calculations. A similar perovskite model with the composition of $FA_{0.5}MA_{0.5}PbI_3$ was used to replace the complex perovskite system to study the chemical interaction between TTA and the perovskite, when the PbI_2-terminal and FAMAI-terminal perovskite slabs were chosen for studying the interaction, respectively. The adsorption energy (E_{ad}) of TTA on the perovskite can be calculated by the energy obtained from first principles according to the relationship of:

$$E_{ad} = [E(\mathrm{TTA}) + E(\mathrm{FA_{0.5}MA_{0.5}PbI_3}) - E(\mathrm{FA_{0.5}MA_{0.5}PbI_3} - \mathrm{TTA})]/S_A,$$

where $E(\mathrm{TTA})$, $E(\mathrm{FA_{0.5}MA_{0.5}PbI_3})$ and $E(\mathrm{FA_{0.5}MA_{0.5}PbI_3} - \mathrm{TTA})$ stand for the total energy of TTA, the perovskite and the TTA-perovskite system, respectively, and S_A refers to the surface area. As Fig. S4† shows, the TTA possesses a large adsorption energy at the surface of the perovskite, whether on the PbI_2-terminal slab or the FAMAI-terminal slab. As Fig. 2d–f shows, the TTA can interact with the PbI_2 plane by the coordination roles between –C=O/thiophenic S and Pb *via* donating or accepting electrons. The detailed interaction between TTA and the PbI_2 slab can be observed intuitively by evaluating the charge density difference on the (100) crystal plane, in which the red/blue areas represent the electron-rich/electron-poor units. In Fig. 2g–i, compared with the PbI_2 slab, the electron density of Pb at the PbI_2/C=O slab and the PbI_2/–S slab increases, indicating the potential charge transfer from –C=O

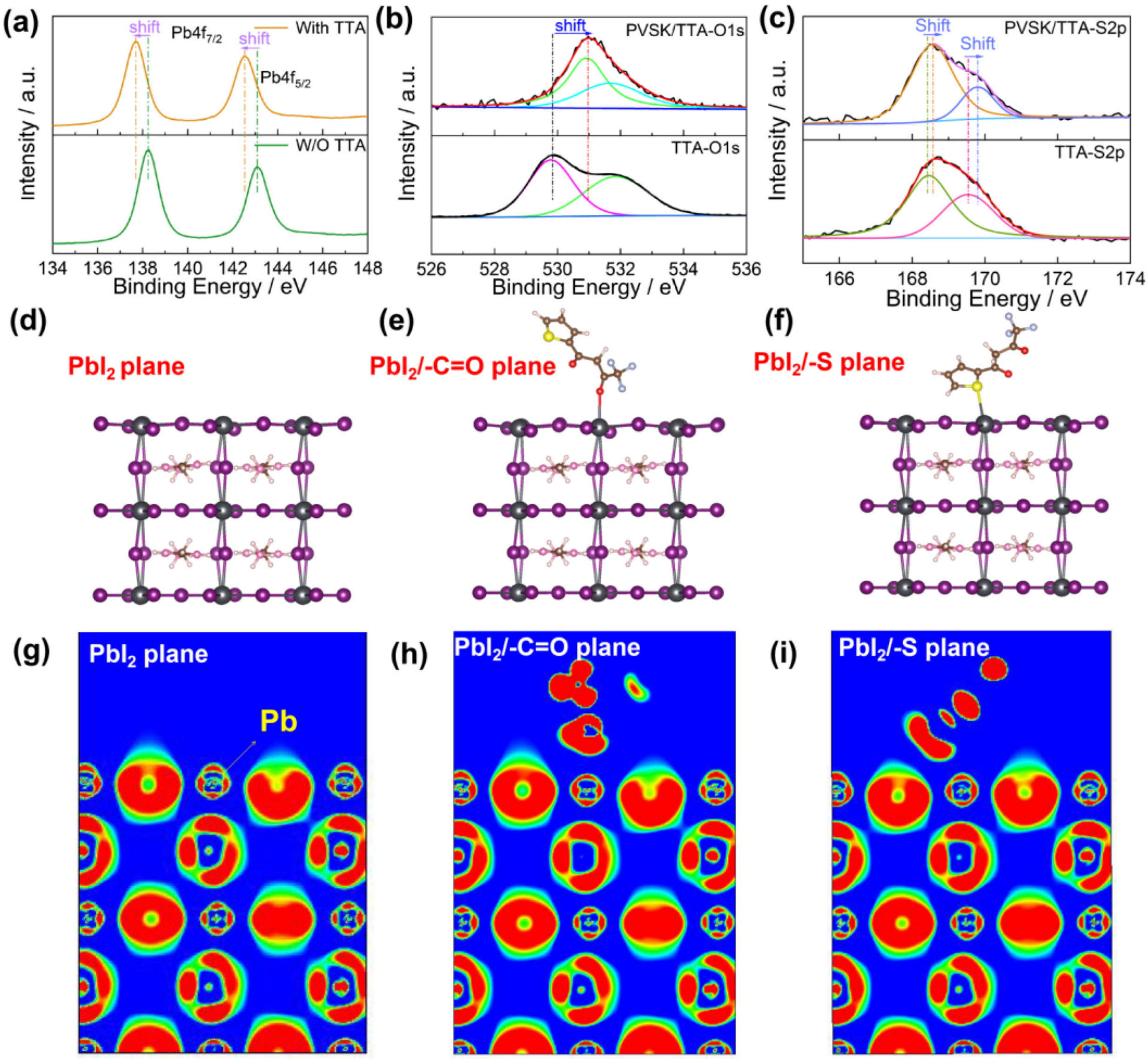

Fig. 2 XPS spectra of (a) Pb 4f, (b) O 1s and (c) S 1s for the perovskite (PVSK), TTA, PVSK/TTA; theoretical model for the interaction between the TTA molecule and the PbI_2-terminal perovskite film with different interaction sites: (d) PbI_2 slab, (e) PbI_2/−C═O slab and (f) PbI_2/−S slab; 2D visual charge density difference of the (100) plane section with isovalue of 0.002 e Å^{-3} for different interaction sites: (g) PbI_2 slab, (h) PbI_2/−C═O slab and (i) PbI_2/−S slab.

and thiophenic S to Pb, which corresponds to the results of XPS and FTIR. A schematic diagram of the interaction between the perovskites and TTA is shown in Fig. S5.† Besides, for the FAMAI/TTA interface in Fig. S6a and b,† the TTA can interact with the FAMAI plane by forming −C═O⋯H and −F⋯H hydrogen bonding. The charge density differences of (100) and (110) crystal planes were selected to study the interaction at the −C═O/perovskite slab and the −F/perovskite slab, respectively. In Fig. S7a, b, S8a and b,† after modifying with TTA, the decreased red color unit indicates that the electron density on H atoms from organic amine decreased. The electrons on H atoms can transfer to −C═O and −F to form hydrogen bonding due to the high electronegativity of O and F, which is consistent with the results of FTIR in Fig. S3.† The theoretical and experimental results above all demonstrate that the TTA can exert interactions with the perovskite.

In order to study the possible interaction between TTA and Li^+, we characterized the XPS and FTIR of TTA, Li-TFSI and TTA/Li-TFSI. In Fig. 3a and Fig. S9,† after introducing the Li-TFSI into the TTA, the characteristic absorption peak of the C═O bond decreased from 1658 cm^{-1} to 1628 cm^{-1}, while no obvious peak position shifts were observed for the absorption peak of the C–S bond from the thiophene ring at 731 nm. Hooke's law shows the vibrational frequency is related to the square root of the bond force constant.[22] The decreased wavenumber of −C═O indicates that the −C═O bond is weakened by the possible coordination between −C═O and Li^+. The unchanged wavenumber of the −C–S bond indicates that there

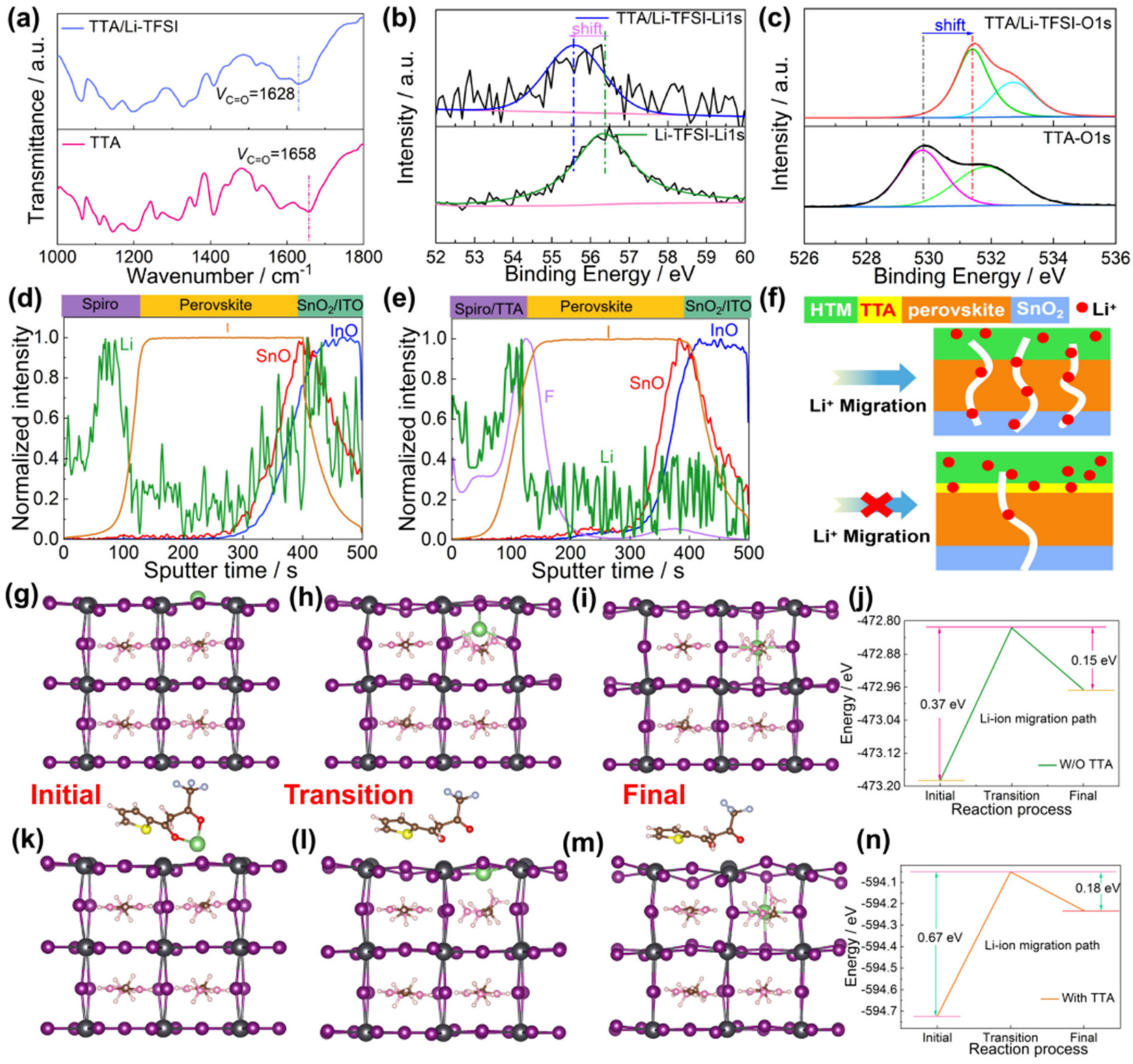

Fig. 3 (a) FTIR spectra of TTA and TTA/Li-TFSI; XPS spectra of TTA, Li-TFSI and TTA/Li-TFSI: (b) Li 1s and (c) O 1s; (d) and (e) TOF-SIMS of Li, I, SnO, F and InO in devices W/O and with TTA modification; (f) schematic diagram of inhibiting Li$^+$ migration from the spiro-OMeTAD to the perovskite and SnO_2 due to TTA; the simulated Li$^+$ migration pathway in a control or TTA-modified device: (g and k) initial state, (h and l) transition state, (i and m) final states, (j and n) corresponding energy barriers.

are no obvious coordination interactions between thiophene S and Li. In Fig. 3b and c, after modifying with TTA, the binding energy of Li 1s decreased from 56.36 eV to 55.59 eV and that of O 1s in –C=O increased from 529.81 eV to 531.41 eV, both of which are sufficient to indicate the strong interaction between TTA and Li$^+$ by donating the electrons of –C=O to Li$^+$. This strong interaction makes it possible for the TTA to inhibit undesired Li$^+$ migration. To verify whether TTA blocks Li$^+$ migration from the HTL to the perovskite, we performed time-of-flight secondary ion mass spectrometry (TOF-SIMS) depth profile characterizations. The devices used for testing were first aged for 200 h under air conditions with a relative humidity of 10–20%. For the control device without TTA modification (see Fig. 3d), the peak of Li$^+$ overlaps with that of I and SnO, illustrating that Li$^+$ is easy to migrate from the HTL layer to the perovskite and SnO_2 layer. For the device with TTA modification (see Fig. 3e), the overlap between Li$^+$ and SnO is greatly reduced, indicating Li$^+$ was mainly located at the spiro-OMeTAD layer rather than migrating into the SnO_2 layer, illustrating the obvious Li$^+$ migration inhibition roles of TTA. As depicted in Fig. 3f, the vast majority of Li$^+$ would be confined to the spiro layer or the spiro/perovskite interface due to the strong interaction between TTA and Li$^+$.

In order to verify the Li$^+$ migration inhibition roles of TTA further, we employed first-principles calculations to simulate and optimize the possible models and Li$^+$ migration pathways based on the $FA_{0.5}MA_{0.5}PbI_3$ perovskite model. In the migration path of Li$^+$, the initial, transitional and final states of Li$^+$ for the device without and with TTA modification are shown in Fig. 3g–i and k–m, respectively, where the initial, transitional and final states of Li^+ were defined by examining whether Li^+ crosses the shared crystal plane between two neighboring perovskite unit cells.[24] According to the respective energies of these three states, we obtained the energy curves of the migration process and calculated the energy barrier of Li^+ migration, as shown in Fig. 3j and n. As Table S1† summarizes, after modifying with TTA, the energy barrier for Li^+ migration increases from its original 0.37 eV to 0.67 eV, revealing the inhibited Li^+ migration due to TTA. The chemical interaction between –C═O and Li^+ can allow one to interpret the suppressed Li^+ migration. Overall, all experiments and theoretical results illustrate that the TTA can suppress the Li^+ migration from the spiro to the perovskite effectively.

The effects of TTA modification on charge carriers in the perovskite films were characterized by photoluminescence spectroscopy (PL) and time-resolved photoluminescence (TRPL) as shown in Fig. 4a and b. The PL intensity of the TTA-modified perovskite film is significantly stronger than that of the control device, which indicates the reduced nonradiative recombination in the perovskite film.[25] According to the bi-exponential function and lifetime formula in eqn (1) and (2), the PL decay was fitted, and the corresponding fitting lifetimes were calculated and are listed in Table S2:†[25]

$$y = A_1 e^{(-t/\tau_1)} + A_2 e^{(-t/\tau_2)} \tag{1}$$

$$\tau_{\text{ave}} = \frac{A_1 {\tau_1}^2 + A_2 {\tau_2}^2}{A_1 \tau_1 + A_2 \tau_2} \tag{2}$$

Here, the A_i (i = 1,2) values refer to the corresponding amplitudes, and the τ_i values represent the fast or slow decay components. The average lifetime (τ_{ave}) of a pure perovskite film is 62.90 ns, while that of the TTA-modified film increases to 117.66 ns. In Fig. S10,† the trap density (n_t) of the perovskite were further measured by space-charge-limited current (SCLC) under dark conditions based on the hole-only device structure of ITO/PEDOT-PSS/perovskite/(TTA)/spiro-OMeTAD/Ag. According to the following eqn (3), the n_t of perovskite films can be calculated from the trap-filled limit voltage (V_{TFL}):[26]

$$n_\text{t} = \frac{2\varepsilon\varepsilon_0 V_{\text{TFL}}}{qL^2} \tag{3}$$

where ε_0 is the vacuum permittivity, ε is the relative dielectric constant of the perovskite, q is the elemental charge and L is

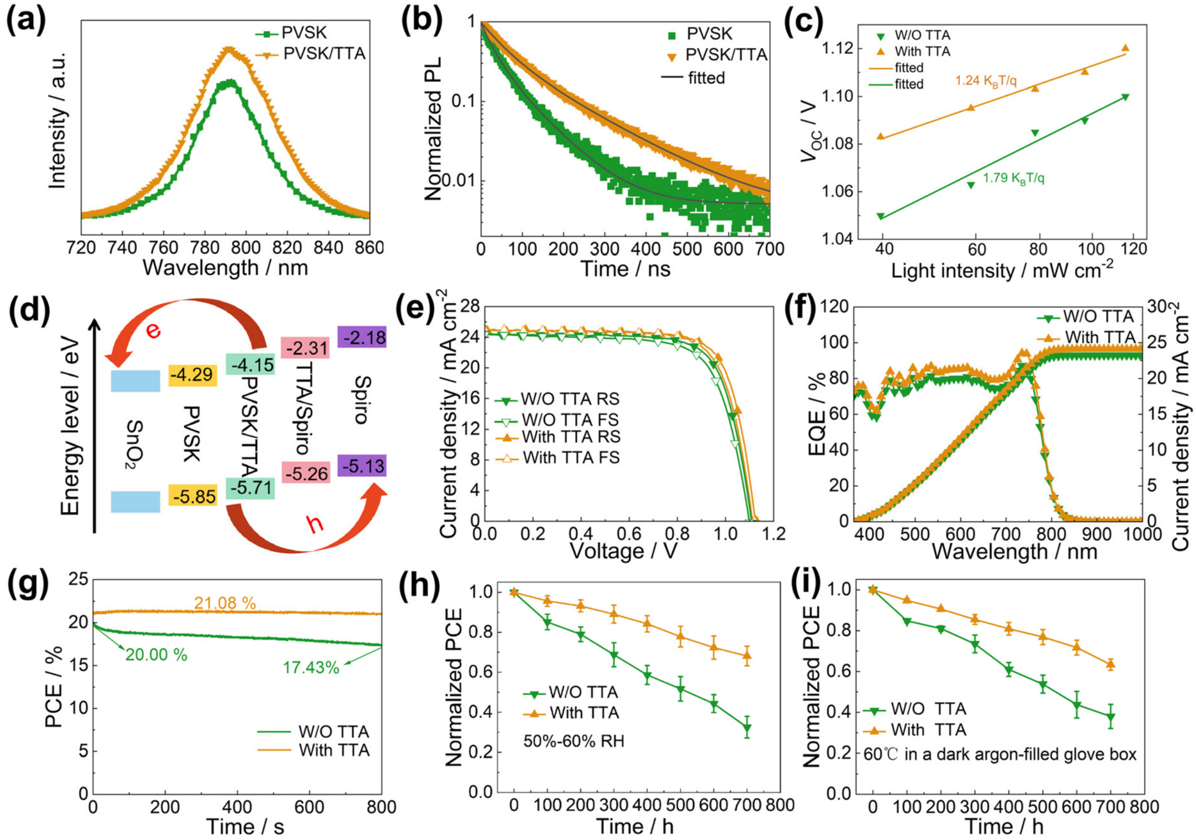

Fig. 4 (a) PL and (b) TRPL spectra for perovskite (PVSK) and PVSK/TTA based on the glass substrate, respectively; (c) light intensity dependent V_{OC} curves of devices W/O or with TTA modification; (d) energy level diagram of PSC; (e) reverse and forward scanned J–V curves; (f) external quantum efficiency (EQE) and corresponding integrated J_{SC} curves; (g) steady-state PCE *versus* time for the best-performing devices W/O and with TTA at the maximum power point; normalized PCE evolution of unencapsulated devices aged at different conditions: (h) under air conditions with a relative humidity of 50%–60%; (i) at 60 °C in a dark argon-filled glove box.

the film thickness, respectively. Because of the defect passivation roles of TTA, the n_t of perovskite films reduces from 8.21 × 10^{15} to 5.12 × 10^{15} cm^{-3}, which can explain the reduced nonradiative recombination caused by TTA.

In order to study the influences of TTA on hole extraction further, we investigated the PL and TRPL characterization based on the spiro-coated perovskite films, as shown in Fig. S11.† The PL measurements reveal that the perovskite coated with spiro and TTA/spiro exhibits significant PL quenching, and the PL quenching of TTA/spiro is the most obvious. As Table S2† summarizes, the average lifetime (τ_{ave}) decreased from 62.90 ns to 41.34 ns and 21.70 ns after coating with spiro and TTA/spiro, respectively. The results of PL and TRPL show that the hole transport and extraction performance of TTA-modified devices was significantly improved.

We measured the light intensity dependence (I) of V_{OC} and J_{SC} for the devices with and without TTA modification. Fig. 4c reveals that V_{OC} shows a linear relationship *vs.* the light intensity dependence (eqn (4)),[27]

$$V_{OC} = \frac{nk_BT}{q}\ln(I) \tag{4}$$

where n represents the ideality factor, and T, k_B and q are Kelvin temperature, Boltzmann constant and elemental charge, respectively. As we all know, the ideal factor (n) can be obtained from the dependence of V_{OC} on light intensity, which can be used to evaluate the recombination process in a perovskite solar cell. Previous reports have indicated that when the n value is between 1 and 2, the non-radiative process caused by Shockley–Read–Hall (SRH) recombination is dominant in the perovskite film, and when n = 1, a diode accounts for an ideal device.[28,29] Therefore, when n is smaller, a device is closer to the ideal device, and the non-radiative coincidence is smaller.[30] After TTA modification, the ideality factor decreased from 1.79 to 1.24, indicating the reduced nonradiative recombination due to TTA. As revealed in Fig. S12,† J_{SC} follows a power law dependence on I ($J_{SC} \propto I^{\alpha}$). After modifying with TTA, the linear fitted exponential factor (α) is closer to 1, proving that the bimolecular nonradiative recombination can be ignored for a TTA-modified device. As electrochemical impedance spectroscopy (EIS) and the equivalent circuit model shown in Fig. S13† demonstrate, the TTA-modified device shows smaller transmission resistance in the high frequency region and larger recombination resistance at low frequency, revealing that TTA can reduce the possibility of nonradiative recombination. The Mott–Schottky curve was used to characterize the relationship between the driving factor of the interfacial hole transport and the built-in potential (V_{bi}). In Fig. S14,† the V_{bi} value of the device with TTA is 0.83 V, higher than that without TTA (0.72 V), which is conducive to reduce the interface charge recombination and promote hole extraction. The built-in potential (V_{bi}) results from the difference in effective work function between the p-type and n-type collection layers, which increases with a decrease in the local injection barrier at these interfaces.[31] Therefore, the increased built-in potential can be attributed to the decreased interface barrier between the perovskite and spiro-OMeTAD modified by TTA, which is evident from the subsequent energy level arrangement diagram. In addition, the results of the dark *J*–*V* curve in Fig. S15† manifests reduced leakage current and carrier recombination loss in the TTA-modified device. Apart from this, the energy level alignment between the perovskite layer and the HTL also plays a crucial role in hole transport and overall device performance for a PSC. Therefore, we performed ultraviolet photoemission spectroscopy (UPS) measurements to explore the effect of the TTA layer on the energy levels of the perovskite and spiro-OMeTAD HTL, and these are shown in Fig. S16 and 17,† respectively. As listed in Fig. 4d, after modifying with TTA, the valence bond (vb) of the perovskite increased from −5.85 to −5.71 eV, and the highest occupied molecular orbital energy level of the spiro-OMeTAD HTL decreased from −5.85 to −5.71 eV, while the highest occupied molecular orbital energy level of spiro-OMeTAD decreased from −5.13 to −5.26 eV. After TTA modification, the energy level alignment of the perovskite and the spiro-OMeTAD layer is more matchable, which is conducive to the collection of photogenerated holes from the perovskite to the spiro-OMeTAD layer with a lower energy loss, so increasing the V_{OC} of devices.

The effects of TTA modification on device efficiency and stability were studied. The current density–voltage (*J*–*V*) curves of the control and TTA-modified target devices were measured under ambient conditions using standard AM 1.5G illumination. In Fig. 4e and Table S3,† the best control device without TTA showed a reverse-scanned PCE of 20.17% with a short-circuit current density (J_{SC}) of 24.50 mA cm^{-2}, an open-circuit voltage (V_{OC}) of 1.11 V and a fill factor (FF) of 74.15%, while a forward-scanned PCE of 19.18% was obtained (J_{SC} = 24.20 mA cm^{-2}, V_{OC} = 1.10 V, FF = 72.04%). In contrast, the best TTA-modified target device has a significantly improved reverse-scanned PCE reaching 22.03% (J_{SC} = 24.99 mA cm^{-2}, V_{OC} = 1.13 V, FF = 78.01%) and forward-scanned PCE of 21.30% (J_{SC} = 24.90 mA cm^{-2}, V_{OC} = 1.12 V, FF = 76.37), outperforming some Cs-MA-FA-based PSCs described in other works (Table S4†). The improved J_{SC} and FF can result from the increased light harvesting and reduced transmission resistance, respectively. The increased V_{OC} can be attributed to the reduced non-radiative recombination and matched energy level assignment provided by TTA. Besides, we also added TTA into spiro-OMeTAD solution and tested the corresponding *J*–*V* curves of devices. As shown in Fig. S18,† the device based on TTA-modified spiro-OMeTAD achieved an efficiency of 18.96%, which is lower than that of the control device (20.17%) and target device (22.03%). Therefore, TTA is introduced into the interface between the perovskite and spiro-OMeTAD layers for better PSC performance.

Hysteresis is another important parameter used to evaluate device performance. The hysteresis index (HI) of a device is calculated using eqn (5):

$$HI = \frac{PCE_{RS} - PCE_{FS}}{PCE_{RS}} \tag{5}$$

where PCE_{RS} and PCE_{FS} represent the PCE in the reverse and forward scans, respectively. As shown in Table S5,† the HI values of devices without and with TTA are 0.05 and 0.03, respectively. The reduced hysteresis effect can be attributed to the Li^+ migration being inhibited by TTA. The EQE spectrum in Fig. 4f proved that the TTA-modified device has a higher integrated J_{SC} (24.11 mA cm^{-2}) than that of the control device (23.25 mA cm^{-2}), which is consistent with the J–V test results. The statistical analysis results of performance parameters given in Fig. S19, 20 and Table S6† showed that the performance of the device is best when the concentration of TTA is 0.4 M. We tracked devices with and without TTA at the maximum power point (MPP) to obtain continuous PCE and J_{SC} results as shown in Fig. 4g and Fig. S21,† respectively, and the voltage of MPP tracking are 0.86 V and 0.83 V for devices with and without TTA, respectively. After 800 seconds, the PCE dropped from 20.00% to 17.43%, and J_{SC} decreased from and 24.10 mA cm^{-2} to 21.50 mA cm^{-2} for the device without TTA modification. In contrast, the TTA-modified device shows relatively stable PCE and J_{SC} values of 21.08% and 24.52 mA cm^{-2}, indicating that TTA modification can improve the optical stability of the device.

To investigate the effect of TTA on resultant device stability, we tracked the photovoltaic performance of unpackaged devices aging under different conditions. By comparing the long-term stability of PSCs in a moisture-proof box (1%–2% RH) and in air (10%–20% RH), as shown in Fig. S22 and 23,† we found the TTA-modified PSCs retained (89.67% and 70.45%) much higher PCE than those devices prepared without TTA (77.60% and 44.44%) after aging over 1200 h. The device stability was further assessed under conditions of higher humidity and temperature. In Fig. 4h, the device with TTA modification retains 69.12% of its initial PCE after aging under air conditions with relative humidity of 50%–60% over 700 h, while the control device preserves only 32.53% of its initial PCE value. The enhanced humidity stability can not only be attributed to the increased contact angle from 82.20° to 85.23° for TTA, as shown in Fig. S24,† but also results from the inhibited Li^+ migration and corresponding negative effects. In Fig. 4i, after heating the devices in an Ar-filled glove box at 60 °C for 700 h, the TTA-modified device maintained 63.35% of its initial PCE, while only 37.97% of the initial PCE value can be maintained for the control device. The normalized evolution trend of J_{SC}, V_{OC} and FF shown in Fig. S25 and S26† also further proved that TTA modification can boost the humidity and thermal stability of the device. These results all proved that the TTA-modified device demonstrated better stability than the control device. The passivated defects, accelerated carrier transmission, reduced recombination and inhibited Li^+ migration due to TTA contributed to enhanced device stability.

Conclusions

In conclusion, we highlight the effect of TTA on Li^+ migration inhibition for highly efficient and stable PSCs. To address this issue, we demonstrated an effective strategy by adding TTA at the perovskite/spiro-OMeTAD interface. The above results showed that TTA could prevent Li^+ migration by coordinating with Li^+ to increase its migration barrier. Meanwhile, thiophene S and diketone in TTA could interact with uncoordinated Pb^{2+} in the perovskite by donating their electrons to Pb^{2+}, which is conducive to passivate the defects and reduce nonradiative recombination in the device. Besides, TTA modification can make the energy-level assignment more matched, which can improve hole extraction efficiency and reduce energy losses. Benefiting from the reduced non-radiative recombination, inhibited Li^+ migration and matched interface energy level, TTA-modified PSCs achieved a best PCE of over 22%. Furthermore, unencapsulated PSCs demonstrated improved stability under constant light, and high temperature and humidity. Our work provides a new direction for inhibiting Li^+ migration in high-performance PSCs.

Data availability

All data are available in the manuscript and in the ESI.†

Author contributions

Y. Ma: investigation, validation, data curation, formal analysis, visualization, writing – original draft. M. Yang: investigation, resources. M. Guo: investigation, resources. Y. Guo: DFT calculations, visualization. Y. Xiao: visualization, supervision, methodology, writing – review and editing. G. Hang: conceptualization, funding acquisition, methodology, supervision, visualization, writing – original draft, writing – review and editing. W. Hou: writing – review and editing, resources, supervision, funding acquisition, project administration.

Conflicts of interest

There are no conflict to declare.

Acknowledgements

This work was financially supported by the National Natural Science Foundation of China (U21A20172, 61804091, and U21A6004), Scientific and Technological Innovation Programs of Higher Education Institutions in Shanxi (2020L0002), and the Natural Science Foundation of Shanxi Province under Grant (201901D211127), the Program of the State Key Laboratory of Quantum Optics and Quantum Optics Devices (No. KF201910). The authors are also grateful for the Scientific Research Start-up Funds of Shanxi University, Hundred Talents Plan of Shanxi Province, Quanzhou "Tong Jiang Scholar" Program, and Fujian Natural Science Funds for Distinguished Young Scholars (2020J06046).

References

1 M. Kim, J. Jeong, H. Z. Lu, T. K. Lee, F. T. Eickemeyer, Y. H. Liu, I. W. Choi, S. J. Choi, Y. Jo, H. B. Kim, S. I. Mo, Y. K. Kim, H. Lee, N. G. An, S. Cho, W. R. Tress, S. M. Zakeeruddin, A. Hagfeldt, J. Y. Kim, M. Grätzel and D. S. Kim, Conformal quantum dot–SnO2 layers as electron transporters for efficient perovskite solar cells, *Science*, 2022, **375**, 302–306.

2 J. F. Liao, W. Q. Wu, Y. Jiang, J. X. Zhong, L. Z. Wang and D. B. Kuang, Understanding of carrier dynamics, heterojunction merits and device physics: towards designing efficient carrier transport layer-free perovskite solar cells, *Chem. Soc. Rev.*, 2020, **49**, 354–381.

3 T. Wang, Y. Zhang, W. Y. Kong, L. Qiao, B. G. Peng, Z. C. Shen, Q. F. Han, H. Chen, Z. L. Yuan, R. K. Zheng and X. D. Yang, Transporting holes stably under iodide invasion in efficient perovskite solar cells, *Science*, 2022, **377**, 1227–1232.

4 U. Bach, D. Lupo, P. Comte, J. Moser, F. Weissrtel, J. Salbeck, H. Spreitzer and M. Grätzel, Solid-state dye-sensitized mesoporous TiO2 solar cells with high photon-to-electron conversion efficiencies, *Nature*, 1998, **395**, 583–585.

5 Q. Lou, G. Lou, H. L. Guo, T. Sun, C. Y. Wang, G. D. Chai, X. Chen, G. S. Yang, Y. Z. Guo and H. Zhou, Enhanced efficiency and stability of n-i-p perovskite solar cells by incorporation of fluorinated graphene in the spiro-OMeTAD hole transport layer, *Adv. Energy Mater.*, 2022, **36**, 2201344.

6 S. G. Kim, T. H. Le, T. de. Monfreid, F. Goubard, T. T. Bui and N. G. Park, Capturing mobile lithium Ions in a molecular hole transporter enhances the thermal stability of perovskite solar cells, *Adv. Mater.*, 2021, **33**, 2007431.

7 Z. Li, C. X. Xiao, Y. Yang, S. P. Harvey, D. H. Kim, J. A. Christians, M. J. Yang, P. Schulz, S. U. Nanayakkara, C. S. Jiang, J. M. Luther, J. J. Berry, M. C. Beard, M. M. A. Jassima and K. Zhu, Extrinsic ion migration in perovskite solar cells, *Energy Environ. Sci.*, 2017, **10**, 1234.

8 G. H. Ren, W. B. Han, Y. Y. Deng, W. Wu, Z. W. Li, J. X. Guo, H. C. Bao, C. Y. Liu and W. B. Guo, Strategies of modifying spiro-OMeTAD materials for perovskite solar cells: a review, *J. Mater. Chem. A*, 2021, **9**, 4589.

9 T. Leijtens, T. Giovenzana, S. N. Habisreutinger, J. S. Tinkham, N. K. Noel, B. A. Kamino, G. Sadoughi, A. Sellinger and H. J. Snaith, Hydrophobic organic hole transporters for improved moisture. resistance in metal halide perovskite solar cells, *ACS Appl. Mater. Interfaces*, 2016, **8**, 5981.

10 H. Y. Bao, H. L. Liu, S. R. Wang, J. F. Ma and X. G. Li, Restricting lithium-ion migration via Lewis base groups in hole transporting materials for efficient and stable perovskite solar cells, *Chem. Eng. J.*, 2022, **433**, 133534.

11 J. S. Luo, J. Q. Zhu, F. Y. Lin, J. X. Xia, H. Yang, J. Y. Yang, R. L. Wang, J. Y. Yuan, Z. Q. Wan, N. Li, C. Brabec and C. Y. Jia, Molecular doping of a hole-transporting material for efficient and stable perovskite solar cells, *Chem. Mater.*, 2022, **34**, 1499–1508.

12 N. D. Pham, J. Shang, Y. Yang, M. T. Hoang, V. T. Tiong, X. X. Wang, L. J. Fan, P. Chen, L. Z. Kou, L. Z. Wang and H. X. Wang, lkaline-earth bis(trifluoromethanesulfonimide) additives for efficient and stable perovskite solar cells, *Nano Energy*, 2022, **69**, 104412.

13 J. B. Zhang, T. Zhang, L. C. Jiang, U. Bach and Y. B. Cheng, 4-tert-butylpyridine free hole transport materials for efficient perovskite solar cells: a new strategy to enhance the environmental and thermal stability, *ACS Energy Lett.*, 2018, **3**, 1677–1682.

14 J. Y. Seo, H. S. Kim, S. Akin, M. Stojanovic, E. Simon, M. Fleischer, A. Hagfeldt, S. M. Zakeeruddin and M. Grätzel, Novel p-dopant toward highly efficient and stable perovskite solar cells, *Energy Environ. Sci.*, 2018, **11**, 2985–2992.

15 Y. Shen, K. M. Deng, Q. H. Chen, G. Gao and L. Li, Crowning lithium ions in hole-transport layer toward stable perovskite solar cells, *Adv. Mater.*, 2022, **34**, 2200978.

16 W. Cao, J. Zhang, K. F. Lin, J. Z. Li, Y. Y. Dong, D. B. Xia, R. Q. Fan and Y. L. Yang, Suppressing glass-transition and lithium-ions migration in hole transport layer by V2O5 decorated graphite carbon nitride nanosheets for thermally stable perovskite solar cells, *Sol. RRL*, 2022, **6**, 2200310.

17 T. Webb, X. P. Liu, R. J. E. Westbrook, S. Kern, M. T. Sajjad, S. Jenatsch, K. D. G. I. Jayawardena, W. H. K. Perera, I. P. Marko, S. Sathasivam, B. Li, M. Yavari, D. J. Scurr, M. R. Alexander, T. J. Macdonald, S. A. Haque, S. J. Sweeney and W. Zhang, A multifaceted ferrocene interlayer for highly stable and efficient lithium doped Spiro-OMeTAD-based perovskite solar cells, *Adv. Energy Mater.*, 2022, **12**, 2200666.

18 W. C. Xiang, S. Z. Liu and W. Tress, Interfaces and interfacial layers in inorganic perovskite solar cells, *Angew. Chem., Int. Ed.*, 2021, **60**, 26440–26453.

19 L. C. Zhang, D. Shi, L. J. Li, X. W. Peng, F. G. Song and H. M. Rui, Solvent extraction of lithium from ammoniacal solution using thenoyltrifluoroacetone and neutral ligands, *J. Mol. Liq.*, 2019, **274**, 746–751.

20 Z. X. Qin, Y. T. Chen, X. T. Wang, N. Wei, X. M. Liu, H. R. Chen, Y. F. Miao and Y. X. Zhao, Zwitterion-functionalized SnO2 substrate induced sequential deposition of black-phase FAPbI3 with rearranged PbI2 residue, *Adv. Mater.*, 2022, **34**, 2203143.

21 Y. Tan, Y. Zhao, L. Wan, L. Y. Lou and Z. S. Wang, Spiro [cyclopentadithiophene-dioxolane]-based D–A–D type organic molecule for both crystallization improvement and band adjustment of Perovskites, *ACS Appl. Mater. Interfaces*, 2022, **14**, 1114–1125.

22 H. B. Chen, Y. J. Ma, X. P. Wang, G. W. Yao, Y. C. Du, J. Y. Zhou, L. Z. Zhu, X. H. Zhao, S. P. Yang, X. P. Liu, M. L. Cai and S. Y. Dai, Improving the stability and efficiency of inorganic CsPbI2Br perovskite via surface reconstruction strategy, *Chem. Eng. J.*, 2022, **442**, 136242.

23 X. Y. Wei, M. Q. Xiao, B. Y. Wang, C. Y. Wang, Y. K. Li, J. Dou, Z. H. Cui, J. Dou, H. L. Wang, S. Ma, C. Zhu, G. Z. Yuan, N. Yang, T. L. Song, H. P. Zhou, H. N. Chen, Y. Bai and Q. Chen, Avoiding structural collapse to reduce lead leakage in perovskite photovoltaics, *Angew. Chem., Int. Ed.*, 2023, **61**, e202204314.

24 J. S. Luo, F. Y. Lin, J. X. Xia, H. Yang, R. L. Zhang, H. A. Malik, H. Y. Shu, Z. Q. Wan, K. L. Han, R. L. Wang, X. J. Yao and C. Y. Jia, An efficient and hydrophobic molecular doping in perovskite solar cells, *Nano Energy*, 2021, **82**, 105751.

25 Q. Cao, Y. K. Li, Y. X. Zhang, J. S. Zhao, T. Wang, B. W. Yang, X. Y. Pu, J. B. Yang, H. Chen, X. Y. Chen, X. Q. Li, S. Ghasemi, H. Salari, A. Hagfeldt and X. H. Li, N-type conductive small molecule assisted 23.5% efficient inverted perovskite solar cells, *Adv. Energy Mater.*, 2022, **12**, 2201435.

26 H. Bi, G. Y. Han, M. N. Guo, C. Ding, H. J. Zou, Q. Shen, S. Hayase and W. J. Hou, Multistrategy preparation of efficient and stable environmentfriendly lead-based perovskite solar cells, *ACS Appl. Mater. Interfaces*, 2022, **14**, 35513–35521.

27 J. L. Duan, Y. Y. Zhao, Y. D. Wang, X. Y. Yang and Q. W. Tang, Hole-boosted Cu(Cr,M)O2 nanocrystals for all-inorganic CsPbBr3 perovskite solar cells, *Angew. Chem., Int. Ed.*, 2019, **58**, 16147–16151.

28 W. Tress, M. Yavari, K. Domanski, P. Yadav, B. Niesen, J. Baena, A. Hagfeldt and M. Graetzel, Interpretation and evolution of open-circuit voltage, recombination, ideality factor and subgapdefect states during reversible light-soaking and irreversible degradation of perovskite solar cells, *Energy Environ. Sci.*, 2018, **11**, 151–165.

29 M. H. Ann, J. Kim, M. Kim, G. Alosaimi, D. Kim, N. Y. Ha, J. Seidel, N. Park, J. S. Yun and J. H. Kim, Device design rules and operation principles of high-power perovskite solar cells for indoor applications, *Nano Energy*, 2020, **68**, 104321.

30 J. J. Zhou, H. Li, L. G. Tan, Y. Liu, J. L. Yang, R. M. Hua and C. Y. Yi, Tuning Hole Transport Properties via Pyrrole Derivation for HighPerformance Perovskite Solar Cells, *Angew. Chem., Int. Ed.*, 2023, **62**, e202300314.

31 C. Li, S. Tscheuschner, F. Paulus, P. E. Hopkinson, J. Kießling, A. Köhler, Y. Vaynzof and S. Huettner, Iodine Migration and its Effect on Hysteresis in Perovskite Solar Cells, *Adv. Mater.*, 2016, **28**, 2446–2454.